Chapter 2

Phase separation kinetics of BCP melts under on-off light cycles

2.1 Introduction

In recent years, there has been a notable increase in interest in using light as a smart stimulus to externally modify and manipulate soft materials [56,60,68–75]. The use of photoinitiated free radical polymerization (FRP) for fabricating soft materials is undeniably a robust and versatile technique [56,57,60,72–77]. This technique governs the design and utilization of next-generation responsive soft materials, enabling numerous advanced biomaterials, coatings, adhesives, and self-healing applications. Additionally, it introduces remarkable innovations in the additive manufacturing of $3d$ printing systems [56,60,74,75]. In these systems, one can utilize photo illumination, which leads to polymerization and cross-linking due to bond breaking in the light on-state while covalently bonding in the off-state of light [56,60,74,75].

Many recent research works study the phase separation kinetics induced by chemical reactions. The resulting morphologies are known as the modulated phase pattern, which results from the competition between chemical reaction and phase separation. The

chemical reactions may be different types leading the polymerization and cross-linking, or it may be a simple reaction like $A \leftrightharpoons B$ [17,78–82]. The competition between phase separation and chemical reaction results in various morphologies, depending on their intensity and spatial distribution [78,79,83,84]. Since the chemical reactions in such systems are typically thermally activated, using light to control the phase separation kinetics is very attractive. However, such studies are mostly unexplored, where photoreactions result in initiation and termination reactions independently of the system's temperature or pressure [80].

The phase separation kinetics in various systems like polymeric solutions, metallic alloys, multicomponent fluids, etc., are well studied [85–87]. The study of phase separation of block copolymers (BCP) has become a topic of ample interest because of its technological importance [63,67,88,89]. Typically, the phase separation process is propelled by the enthalpy of mixing of incompatible blocks, along with entropy that promotes blending. In BCP melt systems, various intriguing morphologies such as spherical, cylindrical, lamellar, and gyroid structures exist, each with different applications across diverse fields. A few essential parameters, including the Flory-Huggins interaction parameter, the volume fraction of the blocks, and the degree of polymerization, drive these domain morphologies [63,67,90,91]. The self-assembly of BCP melts can be controlled by applying external parameters such as electric or mechanical fields [92,93].

Some recent studies focused on the evolution of BCP melt systems forming a series of frozen microstructures [29,94]. Some studies were later conducted using molecular dynamics (MD) [95] and dissipative particle dynamics (DPD) [63,67] simulations to preserve the hydrodynamics in BCP melts. Hydrodynamics accelerates the initial evolution of BCPs, leading to the formation of accurate frozen morphologies. In early times, the segregation was analogous to spinodal decomposition [95], as in polymeric fluids. As time progresses, frozen microstructures form in BCP melts when the domain sizes

are nearly equal to the polymer chain length. As discussed in chapter 1, characteristic domain growth exhibits a crossover from the power law behavior $R(t) \sim t^{1/3}$ to a constant value over time [95].

In this chapter, we have focused on the phase separation kinetics of the BCP melt system in $3d$. The evolving morphologies are tuned by illuminating the system with light, which leads to photo-sensitive reactions. The bond connecting the incompatible beads (A and B) in BCP chains is considered photo-sensitive and, therefore, breaks upon light illumination [56,57,60]. Then, the system behaves as a binary (AB) polymer blend and undergoes macrophase separation when quenched below the critical temperature [23,25]. Conversely, when the light is off, microphase separation occurs in the system due to the bond constraints between incompatible blocks [63,67,95]. The details will be discussed in the next section.

In many reaction-induced phase separation studies, either the equilibrium properties of the system are discussed, or a coarse-grained model relies on uncontrolled approximations for velocity fields [17,81,96–98]. To the best of our knowledge, no simulation studies have addressed the microphase separation kinetics of BCP melts, including photo-controlled reactions under light illumination. However, there is no direct use of light; we can use the same model to break bonds due to deformation in the system or stretching of the simulation box [99–101].

We utilized the DPD simulation technique, as described in Chapter 1, to simulate the BCP melt. We employ the recently developed DPD-based computational approach to simulate controlled radical polymerization (CRP) within polymer networks. The DPD model [59] was validated using previous experiments and simulation studies [102]. The first simulation approach for modeling photo-CRP within polymer networks was developed using the same framework [56,57,60]. DPD proved valuable in the systematic examination of photo initiation, propagation, and termination reactions, leading to the

formation of nanocomposite gels [57] and self-healing gels [56,60]. The results aligned with experimental data [74–76], offering more profound insights into polymerization.

2.2 Photo-controlled reactions mechanism

We have incorporated the effect of light into the DPD model with a consideration of photo-sensitive bonds between incompatible blocks in BCP chains. We consider the two essential reactions: (i) Under light exposure (on-state), the photo-sensitive bonds undergo bond-breaking (initiation) reactions, and (ii) the reformation of broken bonds in the absence of light (termination reactions) [56,57,60]. The other possible reactions are neglected here, like degenerative chain transfer, coupling of same type radical, etc. [56,57,60]. For the bond breaking reactions, we search all photo-sensitive bonds joining *A*-type (blue) and *B*-type (yellow) beads (as we can see in Fig. 2.1). Then, we select the bonds stretched beyond a cutoff length of $r_b = 1.4r_0$ and allow these bonds to break with probability P_b, where $r_0 = 0.5$ is the average bond length [56,57,60]. We select the cutoff value $r_b = 1.4r_0$ to preserve correct first order kinetics, since the values $r_b < 1.4r_0$ leads the deviation from expected behavior and the higher values $r_b \geq 1.6r_0$ slow down the bond-breaking reactions. We set the probability $P_b \in (0.1)$ in our DPD simulation model, which mimics the change in intensity of light illumination. As we increase the intensity, more number of bonds will break and *vice-versa* [56,57,60], and the same principle is applied to P_b in our modeling. After the bond cleavage, the corresponding blue and yellow beads turn into two active radicals, shown in cyan and orange colors.

In the absence of light, the active radicals undergo bond reformation reactions, leading to the regeneration of the BCP chains [56,57]. The active radicals participating in the bond reformation reactions belong to incompatible blocks, and the energy driving this reformation overwhelms the enthalpic difference. Notably, the living free radical polymerization techniques are used in the formation of BCP chains [103,104]. In each

termination reaction, one active radical is randomly selected, after which we examine another active radical of the opposite type within the cutoff radius r_i of the first one. We have taken the optimized value for $r_i = 0.7$ from the previous studies on FRP to ensure the reproduction of correct first-order kinetics [57,59]. We control the bond recombination reactions with probability $P_c \in (0, 1)$. To enable the active radicals to reform the BCP chains, we generate a random number $q \in (0, 1)$ and then compare it to P_c. If $q < P_c$, we accept the reaction; otherwise, we reject it. Each reaction is performed after every 10 DPD time steps, i.e., the time step for each reaction is $\tau_r = 0.2\tau$ [56,59,100].

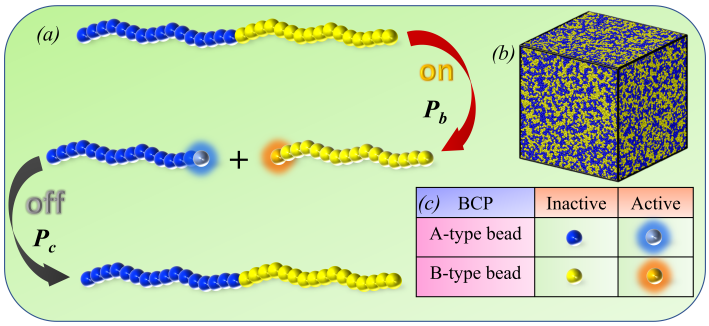

Fig. 2.1: (a) Schematic of bond-breaking and combination reactions during the on- and off-light cycles. P_b and P_c depict the probability of bond-breaking and recombination reactions. (b) The homogeneous mixture of BCP melt system (1 : 1 ratio of A and B-type beads: critical composition) after the equilibration. (c) Representation of color marks of the beads: Inactive A and B-type beads are represented by blue and yellow. At the same time, the corresponding active radicals are shown with glowing cyan and glowing orange.

2.3 System details

We investigate a BCP melt system with system size $L_x \times L_y \times L_z = 64 \times 64 \times 64$ (in reduced DPD units). Along all three directions, the periodic boundary conditions are applied. Since the number density of the system is set to $\rho = 3$, the total number of DPD beads in the system is $N = \rho \times L_x \times L_y \times L_z = 7,86,432$. Each block copolymer chain has $L_p = 32$ DPD beads with 1 : 1 ratio of A and B-type beads, i.e., $N_A = N_B = 16$,

here N_A and N_B represents the number of A-type and B-type beads, respectively. The total number of BCP chains in the system is $N_{pc} = N/L_p = 24,576$.

Our study utilized alternating light cycles, switching on-state and off-state. Each cycle is applied for an equal $t = 600$ time period. To facilitate a comprehensive analysis, we divided our discussion into two sets. Set 1 initiated with the off-state of light (cycle 1), followed by alternating on- and off-cycles applied to the system. Conversely, set 2 commenced with the on-light cycle. Throughout the discussion, we set the bond recombination probability P_c to 1.0 while varying the bond-breaking probability between 0 and 1. This approach allowed us to emphasize the impact of light intensity on evolution, scaling functions, and growth laws.

First, we consider a BCP melt system at high temperature $T = 10$ and equilibrate it for a long time up to $t = 2 \times 10^3$. Then, we quench the system below the critical temperature, reset the time $t = 0$, and observe the domain evolution at various time intervals. Simultaneously, we allow photo-illumination to the system to discuss its effect on the phase separation kinetics of the BCP melt. Here, we will discuss both sets of studies and compare the results for each cycle.

2.4 Effect of alternate light cycles

We will now examine the phase separation kinetics in the BCP melt system using alternating light switching between the on-state and off-state, inducing the bond breaking and recombination reactions. We start with the first set where the sequence of light cycles is off $\rightarrow$ on $\rightarrow$ off $\rightarrow$ on $\rightarrow$ off. We examine the initial cycle at t = 600 to confirm that the system has reached the scaling regimes before initiating subsequent cycles. In the first off-cycles, no reformation reactions occur in the system because of the absence of active radicals. Consequently, a standard microphase separation occurs in the system during the first cycle. The evolution snapshots after the completion of each cycle of

set one are shown in Fig. 2.2; here, the bond breaking probability is set to $P_b = 1.0$ in on-cycles for fixed bond recombination probability $P_c = 1.0$ in off-cycles. The blue and yellow colors represent the A and B-type domains. In cycle 2, bond-breaking reactions occur with probability $P_b = 1.0$. Due to the removal of bond constraints in each BCP chain, the BCP melt system now transforms into a binary polymer blend. As we move from cycle 1 to cycle 2, the kinetics gradually shift from microphase separation in the BCP melt ($P_b = 0$) to macrophase separation in the binary polymer blend ($P_b = 1.0$). Following the macrophase separation in the first on-cycle, the growth gradually slows down due to the formation of A-rich and B-rich macrodomains. Now, the reactions occur only at the interfaces, forming nearly frozen structures in (e) and (f).

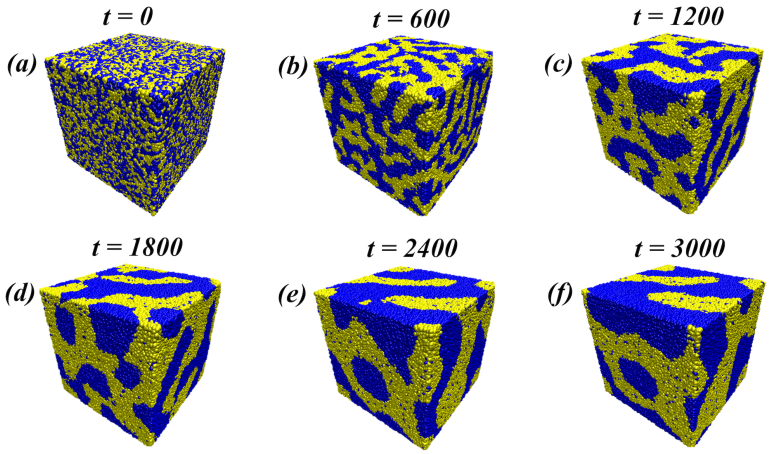

Fig. 2.2: (a) Homogeneous mixture of BCP ($A_nB_n; n = 16$) melt at $t = 0$. (b-f) Subsequent snapshots depict the evolution after each cycle in a sequence of off $\rightarrow$ on $\rightarrow$ off $\rightarrow$ on $\rightarrow$ off. The blue and yellow colors represent the A and B-type beads, respectively.

We compared the evolution for set one at different bond-breaking probabilities shown in Fig. 2.3. After the first cycle, there is no difference, as, during this timeframe, the system undergoes conventional microphase separation without engaging in any photosensitive reactions. In cycle 2, increasing P_b results in the formation of larger domain sizes due to the heightened growth rate of macrophase separation.

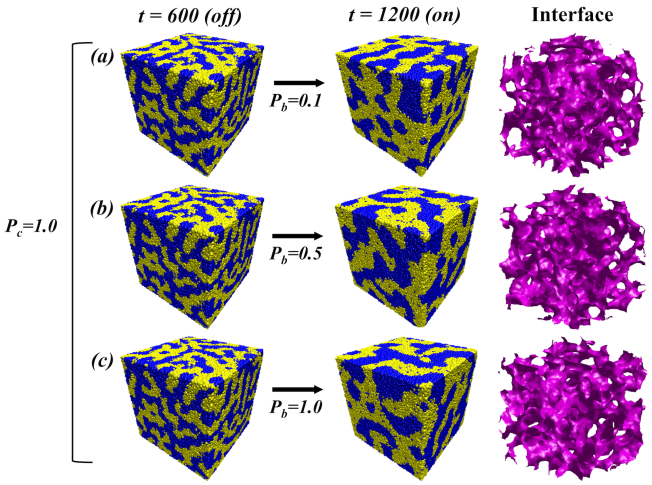

Fig. 2.3: Evolution snapshots for set 1 after the first and second cycles at different bond-breaking probabilities: (a) $P_b = 0.1$, (b) $P_b = 0.5$, and (c) $P_b = 1.0$. The first column depicts the microphase-separated structures at $t = 600$. The second column shows the snapshots after cycle 2. The interface between A and B-type domains is illustrated in the third column at $t = 1200$.

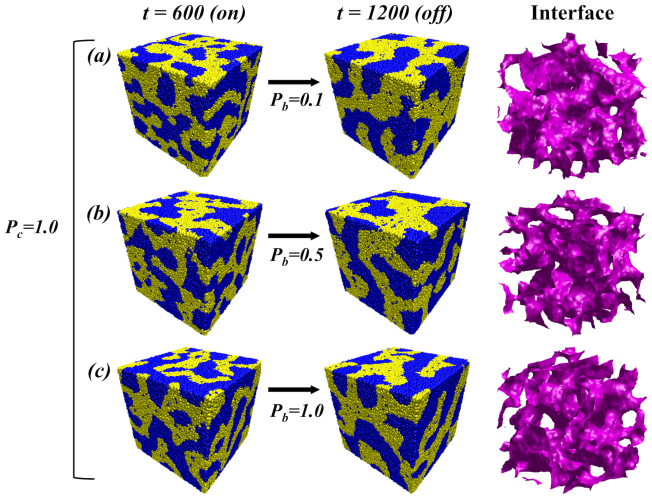

Fig. 2.4: Evolution snapshots for set 2 after the completion of cycle 1 (on) and cycle 2 (off) at different bond-breaking probabilities: (a) $P_b = 0.1$, (b) $P_b = 0.5$, and (c) $P_b = 1.0$. The first column shows the macrophase-separated evolution morphology at $t = 600$. The second column displays the snapshots after cycle two. The interface between A and B-type domains is illustrated in the third column, corresponding to snapshots shown in column two.

In set 2, the phase separation starts with on-light cycle. Consequently, the BCP melt gradually turns into the polymer blend, and spinodal decomposition leads the phase

separation [1,6]. Evolution snapshots for cycles 2 and 3 are depicted in Fig. 2.4 for various light intensities. In cycle 2, the bond recombination reaction commences with $P_c = 1.0$, where the active radicals generated in the preceding cycle reconstruct the BCP chains. The evolution picture depicts a distinct pattern of evolution at $t = 1200$ following microphase separation in cycle 2 at a constant $P_c = 1.0$. This occurs because larger domain sizes have already been established with increasing P_b during the first cycle. However, we can say that the average size of the domains is more significant in set 2.

2.4.1 Reaction kinetics

In our system, the total number of photo-sensitive bonds joining the incompatible blocks of BCP chains is $N_{pc} = 24,576$. To illustrate the impact of light, we compute the cumulative number of bonds cleaved, N_b, during the on-light cycle and the bonds recombined, N_c, during the off-light cycle. First, we normalized these numbers by N_{pc} and plot the corresponding factors n_b and n_c with time in Fig. 2.5. The black and green curves in Fig. 2.5(a) plot the number of broken bonds in on-cycles at $P_b = 1.0$. In the black curve, we observe that $N_b = N_{pc}$ after $t = 100$, indicating that all photo-sensitive bonds have been broken up to this time interval. In cycle 4, we observe $N_b < N_{pc}$ in the green curve. This is due to the trapping of active radicals within large A and B clusters in cycle 2, which results in a lower number of bond reformations in cycle 3 (as indicated by the red curve), leading to $N_c < N_{pc}$. Consequently, fewer bonds break in cycle 4. Increasing the bond-breaking reaction rate enhances the macrophase separation in cycle 2 of set 1, as shown in Fig. 2.5(b) by black ($P_b = 0.1$), red ($P_b = 0.5$), and green ($P_b = 1.0$) curves. Hence, our model accurately captures the impact of varying P_b. In Fig. 2.5(c), we display the time variation of n_b and n_c for various cycles of set 2. We observed similar trends as discussed in Fig 2.5(a). As we progress to higher light cycles,

the number of broken and recombined bonds decreases due to the entrapment of active radicals within the clusters.

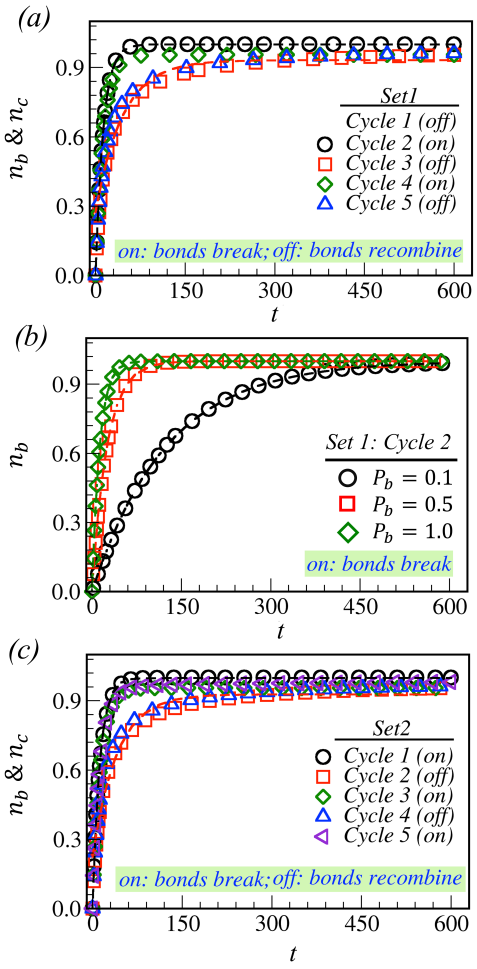

Fig. 2.5: We normalize the cumulative number of bonds broken (N_b) during on-cycles and a cumulative number of bonds recombined (N_c) during off-cycles by the total number of photo-sensitive bonds N_{pc} at $t = 0$. Corresponding normalized numbers are denoted by n_b and n_c, respectively, and plotted as a function of time. (a) Plots for n_b vs. t during on-cycles and n_c vs. t during off-cycles of set 1. (b) Variation of n_b with time for different P_b values for cycle 2 in set 1. (c) Time variation of n_b and n_c corresponding to different cycles of set 2 is plotted with different symbol types. The dashed lines represent the exponential fits, $n_b(t) \sim (1 - e^{-\lambda P_b t})$ followed by each plot, where λ is the fitting parameter.

We have fitted each plot with the exponential equation, $n_b(t) \sim (1 - e^{-\lambda P_b t})$; λ is the fitting parameter for corresponding data, and t is the time interval. We can discuss

a data set plotted in Fig. 2.5(b) for different P_b values. For P_b = 0.1, 0.5, and 1.0, λ have values 0.1, 0.092, and 0.097 respectively. We define the fitting parameter as $\lambda = \Delta t/\tau_r \simeq 0.1$, maintaining a fixed value for different P_b. Nevertheless, variations in τ_r and P_b dictate the rate of bond-breaking reactions. We define the rate constant for the bond-breaking reaction as $k = \lambda P_b$ having values 0.01, 0.05, and 0.1 for P_b = 0.1, 0.5, and 1.0, respectively [100]. Since k has units of τ^{-1}, we can infer that the bond-breaking reaction occurs every k^{-1} = 100, 20, and 10 time intervals for the given P_b values. Therefore, it can be concluded that the bond-breaking reactions belong to a kinetically controlled growth regime because they are slower than the diffusive time scale of DPD simulation [100]. These data demonstrate that our model accurately reproduces the first-order kinetics for bond-breaking reactions [56,57,100]. In our framework, direct utilization of light is not employed; however, altering k simulates an impression of variation in light intensity.

2.4.2 Quantitative study of evolution

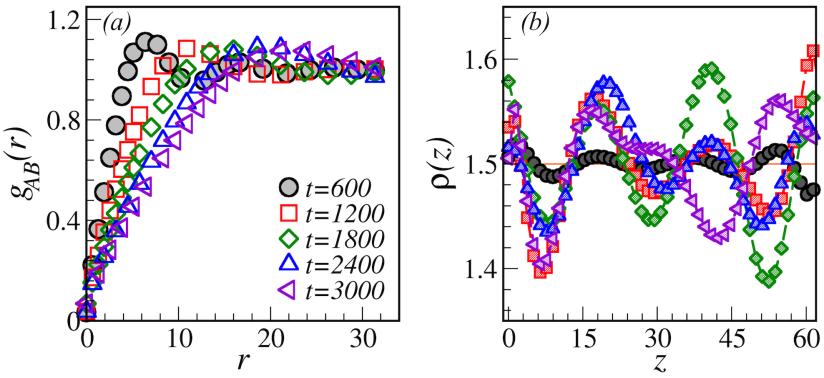

Fig. 2.6: (a) Plots for radial distribution function $g_{AB}(r)$ vs. r after each cycle of set 1. (b) Local number density distribution of A-type beads along z-direction for the same data set plotted in (a) with various symbol types. For each plot, the probability P_b and P_c are fixed at 1.0.

In Fig. 2.6(a), we compare the RDF after the completion of different light cycles of set 1; corresponding morphologies are displayed in Fig. 2.2. During the first cycle,

microphase separation occurs due to the off-state of light. This can be verified by the multiple oscillatory peaks present in the black curve. In the green and purple curves, we expect to see secondary peaks. However, these peaks disappear even during the off-light cycle. Since the evolution in BCP melt is a very slow process, it may require much more time to develop the periodic domains after already formed macrodomains in cycle 2. Hence, the secondary peaks disappear because of the shorter time assigned to evolution once bonds are reformed. The peak position shifts towards higher r values, representing further domain growth with time. To verify the distribution of evolved clusters over time as depicted in Fig. 2.2, we plot the local number density distribution of A-type beads along z-direction in Fig. 2.6(b). The increased width and height of the curves confirm the growth of A-rich clusters over time.

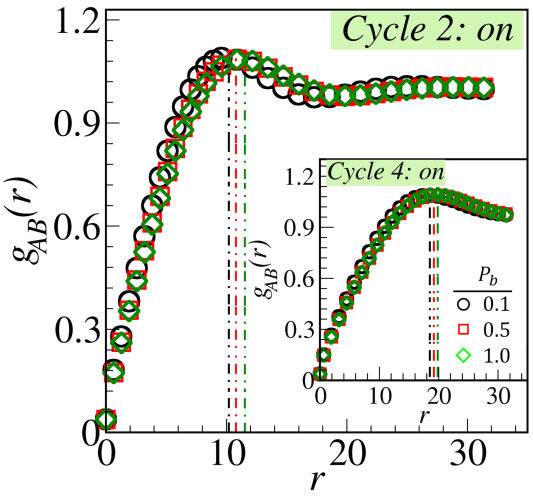

Fig. 2.7: Comparison of $g_{AB}(r)$ vs. r for different probabilities in cycle 2 (on-cycle) of set 1. The inset plot shows the RDF for cycle 4 (on-cycle) with different P_b values indicated by different symbols as specified in the legends.

During the on-light cycles, the increase in P_b results in a faster rate of bond-breaking reactions. Hence, the system rapidly transforms into the binary polymer (AB) blend with a chain length $l_{pc} = 16$. Fig. 2.7 displays the radial distribution function (RDF) for cycles 2 and 4, showcasing various bond-breaking probabilities. The shift in peak position towards larger r for higher P_b values confirms the presence of fast evolution.

We observe the analogous behavior in the RDF curves for on-cycles of set 2. However, during off-cycles, the recombination probability is set to 1, resulting in $g_{AB}(r)$ curves showing a good overlap in peak positions (results are not displayed here).

2.4.3 Characterization functions

Now, we compare the scaled correlation function $C(r,t)$ vs. $r/R(t)$ and the structure factor $S(k,t)$ vs. $kR(t)$ at the end of each cycle of set 1 (see Figs. 2.8(a) and 2.8(b)). We examine the morphology evolution during on- and off-state of light depicted in Fig. 2.2. The black curve ($t = 600$) and the red curve ($t = 1200$) show a significant deviation in the correlation function and structure factor. This deviation could be due to the different kinetics of the system in the two cycles. In the first cycle, with the light-off (no reaction involved), the microphase-separated structures are characterized by the oscillatory nature of the correlation function (black curve in Fig. 2.8(a)) and the appearance of a secondary hump in the structure factor data (black curve in Fig. 2.8(b)). In cycle 2, the macrophase separation occurs via spinodal decomposition due to bond-breaking reactions. After cycle 2 (cycle three and onwards), we notice a good overlap in scaling function data, indicating the formation of the equivalent morphologies. At later times, their statistical properties become independent of the light's on-and off-states, thus belonging to the same class of universality. During the off-light cycles, slower microphase separation occurs due to the restoration of covalent bonds. As in the first on-cycle, larger domains are already formed. Therefore, the time duration allowed for the off-cycles is insufficient to affect the length scale of the system. This could explain the excellent overlap in scaling functions at later times. However, the structure factor plotted in Fig. 2.8(b) shows the expected Porod's law $S(k,t) \sim k^{-(d+1)}$ for $k \to \infty$ as a result of the scattering off sharp interfaces, here $d = 3$ is the dimensionality of the system.

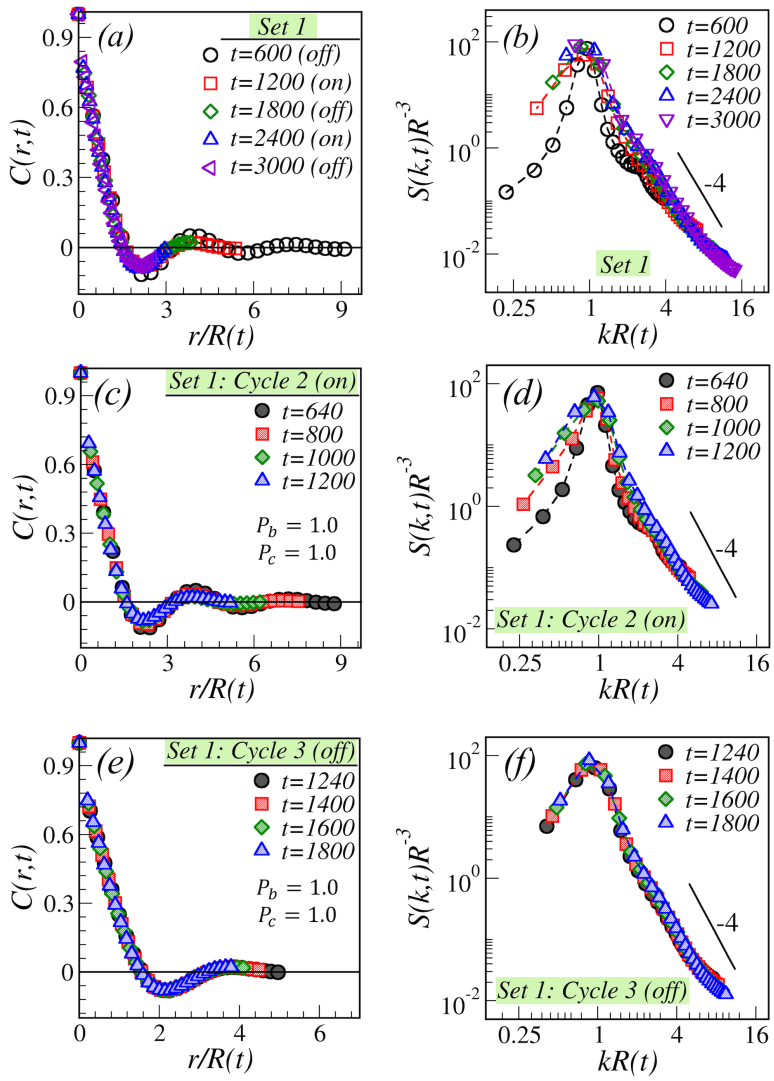

Fig. 2.8: (a) and (b) plots the spherically averaged scaled correlation function and corresponding structure factor after the completion of different on- and off-light cycles in set 1. Various symbol types represent the data at different time intervals. The solid line in (a) depicts the zero crossing of the correlation function. The tail of the structure factor follows Porod's law, illustrated with a solid black line in (b) with slope -4. (c-d) Scaled correlation function $C(r,t)$ vs. $r/R(t)$ and the structure factor $S(k,t)$ vs. $kR(t)$ for different time intervals in cycle 2 set 1 (light-on). (e-f) Same set of observables plotted in (c) and (d) for cycle 3 set 1 (light-off).

In Figs. 2.8(c)-2.8(f), we display the dynamic scaling functions during the first two cycles of set 1, where light stimulated the chemical reaction, keeping $P_b = P_c = 1.0$, i.e., cycles 2 and 3. In cycle 2, a slight deviation from the scaling behavior is noted for

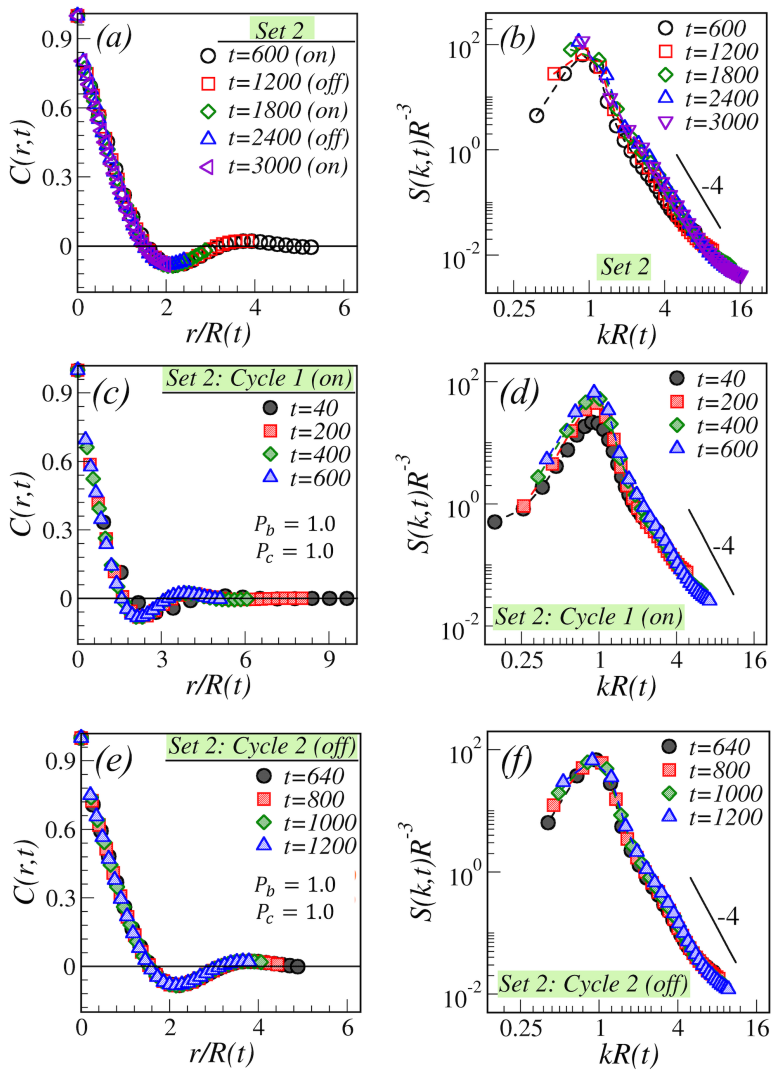

Fig. 2.9: (a-b) Scaled correlation and structure factor after ending each light cycle for set 2. Various symbol types represent the different time intervals. (c-d) Plots for $C(r,t)$ vs. $r/R(t)$ and $S(k,t)$ vs. $kR(t)$ for the evolution through cycle 1 set 2 (bond-breaking on). (e-f) Same set of observables as in (c) and (d) for the evolution through cycle 2 set 2 (bonds are recombining).

early times, as seen in black ($t = 640$) and red ($t = 800$) curves. Up to this time, the kinetics is typically chemically controlled due to bond-breaking reactions. However, an excellent scaling is observed later in green ($t = 1000$) and blue ($t = 1200$) curves. In cycle 3, the bond recombination reaction occurs with probability $P_c = 1.0$. In Fig. 2.8(e) and 2.8(f), an excellent data overlap in both scaling functions reveals an excellent scaling

in the system at each time interval. These findings suggest that the initial on-cycle has a significant impact on the scaling functions. However, when the kinetics resemble spinodal decomposition in binary polymer blends during late time intervals, the scaling behavior is fully preserved.

In Figs. 2.9(a) and 2.9(b), we compare the scaled correlation function $C(r,t)$ vs. $r/R(t)$ and corresponding structure factor $S(k,t)$ vs. $kR(t)$ after the completion of different cycles of set 2 (on $\rightarrow$ off $\rightarrow$ on $\rightarrow$ off $\rightarrow$ on). A deviation from the scaling function is noted in the first on-cycle (black curve at $t = 600$). The well-defined scaling behavior is observed after the system evolves through the first on-state. This verifies our previous observations that domain growth follows the same class of universality irrespective of the on-state and off-state of light after the first on-cycle. Tails of the structure factor follow the well-known Porod's law illustrated by a solid black line with slope of -4.

In Figs. 2.9(c)-2.9(d), we plot $C(r,t)$ vs. $r/R(t)$ and corresponding $S(k,t)$ vs. $kR(t)$ for different time steps in cycle 1 of set 2. Similar to the first on-cycle in set 1, the deviation from the scaling behavior is noted in black ($t = 40$) and red ($t = 200$) curves for the chemically controlled regime. However, the green ($t = 400$) and blue ($t = 600$) curves display the ecellent scaling. In Figs. 2.9(e) and 2.9(f), the same data set is plotted for cycle 2. After the evolution in the first on-cycle, scaling functions have good overlap. The results are analogous to set 1, concluding that the first on-cycle plays a significant role in the system's evolution.

2.4.4 Growth laws

The most interesting outcome is the time-dependent characteristic domain growth. In Fig. 2.10 we plot $R(t)$ vs t for set 1. Fig. 2.10(a) displays the data for all off-cycles, whereas Fig. 2.10(b) presents the data for on-cycles. During cycle 1, microscopic phase

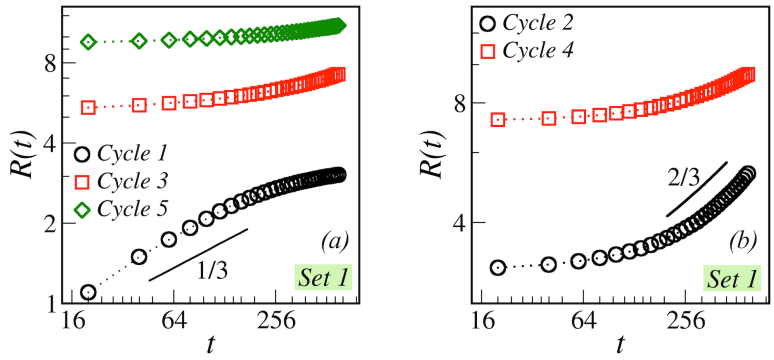

Fig. 2.10: (a) Average domain size $R(t)$ vs. t is plotted for microscopic domain growth during off-cycles (1, 3, and 5) of set 1 when bond recombination reactions reform the BCP chains. A solid black line represents the expected diffusive growth ($\phi \sim 1/3$) at early times. (b) Plots for average length scale $R(t)$ vs. t during macroscopic domain growth in cycles 2 and 4, when bond-breaking reactions turn the BCP melt system into a binary polymer blend. The solid line displays the inertial hydrodynamic growth ($\phi \sim 2/3$) for $d = 3$ fluids.

separation occurs in the system, as no photo-sensitive reaction takes place. Consequently, the black curve in Fig. 2.10(a) follows the diffusive growth ($\phi \sim 1/3$) for a limited time window. The length scale exhibits a cross-over to saturation at later time intervals, indicating the evolution of the frozen microphase. When light illumination is introduced in cycle 2, the system behaves like a binary polymer blend due to bond-breaking reactions. The corresponding black curve in Fig. 2.10(b) shows a gradual cross-over to inertial hydrodynamic growth ($\phi \sim 2/3$), illustrating the macrophase separation during the on-cycle. Since a significant length scale is already reached in cycle 1, the viscous hydrodynamic growth ($\phi \sim 1$) is very short-lived in this case. In subsequent off-cycles (cycles 3 and 5), the curves follow the same trend observed in cycle 1. However, due to the macrodomains already formed in previous on-cycles, saturation is not achieved within the given time interval. In Fig. 2.10(b), the red curve shows relatively slower growth in cycle 4, as the inertial hydrodynamic growth was already achieved in the previous on-cycle.

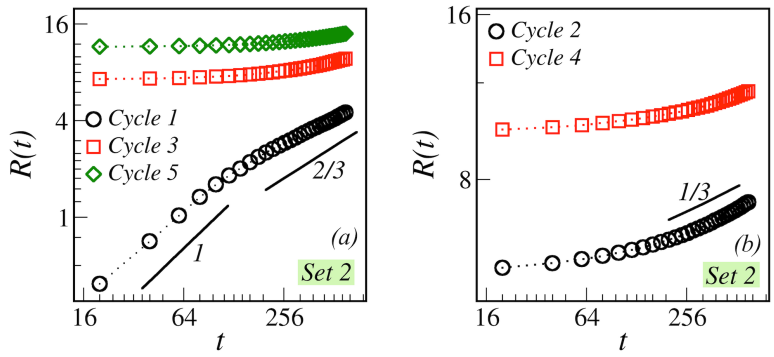

Fig. 2.11: Logarithmic plots for the average domain growth $R(t)$ as a function of time. Data corresponding to on-cycles (1, 3, and 5) of set 2 are plotted in (a) while (b) plots the data for off-cycles (2 and 4). Solid lines represent the growth laws followed by the system in different cycles.

In set 2, the phase separation starts with an on-cycle. The characteristic length scale of different cycles of set 2 is plotted in Fig. 2.11. The black curve in Fig. 2.11(a) follows the expected inertial hydrodynamic growth ($\phi \sim 2/3$) after early time viscous hydrodynamic regime ($\phi \sim 1$). This behavior represents the macrophase separation in the first on-cycle of set 2. As we move towards cycle 2, the black curve in Fig. 2.11(b) follows the diffusive growth at the late time, depicting the microphase separation. The higher on-cycles (3 and 5) exhibit inertial hydrodynamic growth ($\phi \sim 2/3$), while cycle 4 displays diffusive growth ($\phi \sim 1/3$) at later times. As up to cycle 2, the macroscopic growth is already attained; the growth in higher cycles is slower compared to cycles 1 and 2.

2.5 Summary and discussion

In this chapter, we investigated the phase separation kinetics of the BCP system under alternating on- and off-light cycles, which induce bond-breaking and bond-recombination reactions, respectively. The DPD simulation method is used to simulate the system. We extensively examined the impact of light cycles on the evolution, scaling function, and growth laws for two distinct scenarios.

We observed that the rate of bond-breaking can be controlled by varying P_b. We recorded the number of bonds broken and recombined during on- and off-light cycles, normalized by the total number of photo-sensitive bonds in the system. Our model accurately captures the first-order kinetics, which arises from the change in the rate constant k, that mimics the effect of varying light intensity during the on-cycle. In higher on-cycles, the number of broken bonds slightly decreases due to the trapping of active radicals within the domains via reversible radical deactivation in previous off-cycles.

The shift in peak positions of $g_{AB}(r)$ towards higher r values further indicates the formation of more segregated domains at higher k values. This suggests that the higher k values accelerate macrophase separation due to rapid bond-breaking during on-state of light. A perfect overlap in RDF data is noted during the off-cycles because P_c is set to 1.0 in all off-cycles for P_b values from previous on-cycles. Remarkably, any variation in the peak position observed during the previous on-cycle at three different P_b values is nullified within the specified time limit of the off-cycles.

In set 1, the kinetics of the first two cycles are markedly different: the system behaves as a typical BCP melt in cycle 1 and acts as a binary polymer blend in cycle 2. Consequently, the correlation and the structure factor plotted for the first two cycles exhibit a significant deviation from any master function. After cycle 2, both scaling functions exhibit excellent overlap in the data, indicating the formation of statistically similar morphology. The outcome suggests that the evolution in higher cycles is independent of applied light cycles and thereby belongs to the same class of universality. In set 2, the phase separation started with on-light cycle, and the scaling functions have well-fitted behavior at the end of each cycle. Overall, the first cycle determines the scaling behavior for the subsequent cycles. The evolution after the first on-cycle follows the same universality class, regardless of the on- and off-light sequence. The same applies to the scaling functions, where deviations

occur at early times until the first on-cycle, which controls the reaction kinetics with bond-breaking reactions.

From the average domain size plots, we notice larger values in set 2, where the phase separation is started with on-cycle. Corresponding data show more pronounced values at higher light intensities. In set 2, a crossover from viscous ($\phi \sim 1$) to inertial ($\phi \sim 2/3$) hydrodynamic growth indicates the macroscopic phase separation in cycle 1. In the higher on-cycles, the length scale gradually approaches the same growth regime ($\phi \sim 2/3$), as the inertial regime is already established in the first on-cycle. However, when phase separation begins with the off-cycle (set 1), the on-cycles also display the inertial regime at later times after a prolonged transient regime of the respective on-cycle. In contrast, the off-cycles exhibit gradual diffusive growth ($\phi \sim 1/3$) in a limited time window.

The morphologies obtained in various block copolymers (BCPs) hold significant technological importance. These findings are expected to garner further attention and offer a comprehensive framework for analyzing simulation and experimental works on the responsive growth of nanostructures in BCP melts.

In continuation to this chapter, we study the effect of light on the phase separation kinetics of polymer fluids in chapter 3. In that study, we have applied random photo-illumination to the system with different bond-breaking probabilities $P_b \in (0, 1)$ for a fixed bond-recombination probability $P_c = 1.0$.